

INITIAL OXIDATION STAGE OF SiMo AND SiNb-xAl DUCTILE CAST IRONS IN AIR AND CO₂-CONTAINING ATMOSPHERES

Gülşah Aktaş Çelik, Ş. Hakan Atapek and Şeyda Polat

Department of Metallurgical and Materials Engineering, Kocaeli University, 41001 Izmit, Kocaeli, Turkey

Copyright © 2022 American Foundry Society
<https://doi.org/10.1007/s40962-022-00883-w>

Abstract

In this study, novel SiNb-xAl (x:0–4 wt.%) ductile cast irons were developed to be used as exhaust manifold material. Initial oxidation stages of these alloys were studied at 800 °C in air and in a gas atmosphere (9 % CO₂, 4 % O₂ and 87 % N₂) and compared with a commercial SiMo ductile iron. It was found that the newly developed ductile cast irons had higher oxidation resistance compared to the SiMo ductile iron under the studied test conditions, and this resistance increased further, as aluminum content of the ductile cast iron increased. Both surfaces and cross sections of the oxidized cast irons were characterized by 3D profilometer, scanning electron microscope equipped with energy-dispersive spectrometer and X-ray diffraction technique. Dense Fe-rich nodules and an

extremely thick bilayer scale were detected on the surface of the SiMo ductile iron in both test environments. However, the number of nodules on the surface and their distribution frequency were decreased in SiNb cast iron. Aluminum addition to SiNb cast iron caused a further reduction in the number of nodules and also a finer scale formation due to the presence of an Al-rich protective layer on the surface. All these findings are encouraging that new cast irons can be used as alternative materials to SiMo ductile iron.

Keywords: SiMo ductile iron, exhaust manifold, oxidation, characterization

Introduction

More efficient engines working at higher temperatures are needed in automotive industry due to stringent regulations related with exhaust gas emissions.^{1–3} This brings the need for engine components that have high temperature corrosion resistance and superior mechanical properties especially for the exhaust manifold that is subjected to the highest temperature in the exhaust system.^{4–6}

Conventional exhaust manifold materials are iron-based alloys having either austenitic or ferritic matrix. Among these materials, austenitic (CF8C) and ferritic (AISI 409) cast stainless steels are mainly used at higher temperatures due to their high microstructural and mechanical stability.^{7–11} Austenitic (Ni-resist) and ferritic (SiMo) ductile cast irons are also used as exhaust manifold materials,^{12–15} and even though austenitic matrix provides similar high temperature properties as cast stainless steels, ferritic

matrix has limitations due to low A₁ temperature which is about 825 °C,^{4,16} but mostly preferred due to its lower cost.^{3,16,17} Thus, there are many studies comparing the high temperature performance of ferritic ductile cast iron (especially SiMo) with austenitic ferrous-based materials^{3,18,19} and the findings indicate that even though SiMo ductile iron has good potential as an exhaust manifold material its high temperature mechanical properties and oxidation/corrosion resistance need to be improved. In this respect, both Si and Mo contents are varied^{20–22} and alloying elements^{23–27} are used which affect the microstructural features (amount and nodularity of graphite phase)²⁰ and mechanical properties.²⁸ Recent studies have focused on the modification of SiMo compositions by Ni,²³ Cr,^{23–25} Al^{25–29} alloying elements. Although Ni decreases A₁ temperature,³⁰ its addition improves mechanical properties and at limited additions the oxidation resistance of ductile cast irons is enhanced at room temperature.²³ The limited Cr and Al additions both increase A₁ temperature²⁰ and provide high oxidation resistance by forming Cr/Al oxide layers on the metal surface at the elevated temperatures.^{23,24,31} Lekakh *et al.* studied the Cr effect on the

oxidation behavior of 3.2 C- 4.55 Si- 0.94 Mo- 1.05 Cr (wt.%) at 800–1000 °C in air and they reported that Cr addition increased the oxidation resistance by forming Cr-rich oxides on the surface. However, above 1 wt.% Cr addition the alloy became brittle due to the formation of Cr-rich carbides.²⁴ Several studies on the effect of Al alloying on SiMo have revealed that A₁ temperature has considerably increased up to 1000 °C as the aluminum content increased.^{20,32} It has also been reported that both content and morphology of graphite phase are strongly affected by aluminum addition. A morphological change from nodular to vermicular is observed and the amount of graphite embedded in ferritic matrix has decreased as aluminum content increased.^{17,20} Ibrahim *et al.* observed hardness increase and ductility decrease in aluminum-modified cast irons due to solid solution hardening provided by high solubility of aluminum in ferritic matrix.²⁶ Since Al-rich oxides form on the metal surface by aluminum addition, cast irons modified by aluminum are reported to exhibit superior oxidation resistance in air at elevated temperatures.^{24,25} Apart from the studies focusing on modification of SiMo by alloying, Mo-free ductile cast irons are designed by Aktaş Çelik *et al.* in order to eliminate adverse effects of molybdenum, like decreasing A₁ temperature and causing carbide precipitation at the cell boundaries during solidification.^{33–36} In the new alloy design, Nb (1 wt.%) is added to replace molybdenum to attain higher A₁ temperature and aluminum is also added up to 4 wt.% to benefit from its positive effects on the microstructural, mechanical properties and for protection against oxidation at elevated temperatures.^{35,36}

Oxidation tests of cast irons used as exhaust manifolds, carried out in air atmosphere at high temperatures, have revealed considerable information on the surface formations like oxides within the outer/inner layers and decarburization.^{23,24,36–39} During oxidation, inward diffusion of oxygen and outward diffusion of iron determine the scale characteristics consisting of inner and outer layers.^{19,20} While FeO (wustite) and Fe₂SiO₄ (fayalite) oxides form at the inner layer, Fe₂O₃ (hematite) and Fe₃O₄ (magnetite) form at the outer layer of SiMo ductile iron.^{20,23} Among these oxides only Fe₂SiO₄ phase has a protective potential; however, it is not sufficient at elevated temperatures.²³ Besides the formation of these oxides, decarburization also takes place due to the reaction between oxygen and carbon in both graphite and ferrite phases.²⁴ During decarburization, CO/CO₂ forms as a result of oxidation of carbon and the gaseous product is transported through cracks and voids within the scale.¹⁹ The morphology and distribution of graphite phase embedded in ferrite matrix control both oxidation and decarburization kinetics, since graphite phases act as transfer routes for oxygen during these reactions.^{20,36} Stable oxides (CrO₂, Al₂O₃, etc.) of alloying elements like Cr and Al which are less noble than Fe, play an important role in enhancing oxidation resistance of modified SiMo ductile irons as well.^{23,24,27} Oxidation

studies performed in exhaust gas atmosphere have revealed increased oxidation kinetics compared to the air atmosphere due to the presence of oxidizing gases like H₂O, CO₂ and O₂ in the exhaust gas. As a result of the reactions between metal surface and these gases, a continuous oxide layer is formed on the surface that grows faster compared to air atmosphere.²³ Oxidation tests of SiMo and Ni-resist cast irons in dry exhaust gas atmosphere have revealed slower oxidation rates due to the absence of H₂O; however no significant change is observed in oxide formations.¹⁹ Similar to the air atmosphere, both inner and outer layers are observed, and the outer layer is formed by Fe₂O₃ and Fe₃O₄ while in the inner layer FeO, Fe₂SiO₄/SiO₂ oxides are present.^{19,23,24,38,40} The presence of gases like SO_x, N₂ ve NO_x in the exhaust gas cause the formation of FeSO₄, FeS₂ in the oxide layer, at the same time they cause the precipitation of Si₃N₄ in the ferritic matrix and MgSiN₂ at the eutectic cell boundaries of ductile cast iron.^{18,19,40}

There are studies on the oxidation behavior of modified ductile cast irons in several gas atmospheres and the effect of alloying elements like Cr, Ni and Al on the oxidation resistance of SiMo.^{4,23,24} Compared to air environment, exhaust gas causes faster formation of Fe-oxide islands on the SiMo surface and the formation kinetics of SiO₂ that acts as a barrier layer at the interface is slower.^{23,24} When the effect of alloying elements on oxidation behavior of SiMo in exhaust gas atmosphere is considered, (i) Cr addition causes more distinct silica layer and other protective Cr-oxides²³ at the same time suppresses decarburization,²⁴ (ii) Al addition stabilizes the formation of Al-rich oxides inhibiting oxidation and (iii) Ni addition does not provide any contribution in oxidation resistance since it does not cause the formation of compact and continuous SiO₂ layer. All these findings reveal that alloying has a distinctive effect on the oxidation behavior of ductile cast iron both in air and exhaust gas atmospheres. In our previous studies, a novel cast iron composition (SiNb-xAl) has been investigated comparatively with SiMo in terms of its microstructural features,³⁵ physical properties³⁵ and oxidation performance in air atmosphere.³⁶ However, no data have been reported yet on its initial stage of oxidation in CO₂-containing atmosphere. In this study, it is aimed to compare the oxidation behavior of SiNb-xAl cast irons with SiMo in both air and selected gas atmospheres, at 800 °C which is under the A₁ temperature.

Material and Methods

SiMo ductile cast iron commercially used as exhaust manifold material and SiNb-xAl cast irons designed as alternative materials are produced as ½ inch Y block by sand mold casting according to ASTM A 536 - 84 standard. In the casting procedure 5 kg charge is prepared using nodular pig iron (4.30 wt.% C, 0.70 wt.% Si, 0.06 wt.% Mn, 0.05 wt.% P, 0.018 wt.% S), ferrosilicon (0.10 wt.% C,

72 wt.% Si, 0.020 wt.% P, 0.024 wt.% S), ferroniobium (0.20 wt.% C, 2.61 wt.% Si, 0.126 wt.% P, 0.09 wt.% S, 0.87 wt.% Al, 67.80 wt.% Nb) and DIN 1020 steel (0.24 wt.% C, 0.20 wt.% Si, 0.50 wt.% Mn, 0.030 wt.% P, 0.020 wt.% S). An Inductotherm induction furnace (35 kW) with the capacity of 25 kg is used to melt the charge and pure aluminum is added according to the chosen composition just before the melting process is complete. The total amount of the melts produced is 5 kg. After melting is completed at 1560 °C, spheroidization process is carried out in a SiC crucible. For this purpose, nucleation agent (75 wt.% Si, 0.94 wt.% Ca, 1.68 wt.% Ce, 0.89 wt.% Al) and magnesium rich alloy FeSiMg (45 wt.% Si, 7 wt.% Mg) are placed at the bottom of the crucible, then the charge is poured on them. In order to verify the chemical composition, a sample from the molten alloy is taken by pouring it into a copper mold and analyzed using Optical Emission Spectrometer (OES, Foundry Master). The chemical compositions of the cast alloys and their carbon equivalent (C_{eq}) values are given in Table 1. In the compositions, carbon and silicon contents are kept constant to attain the same C_{eq} value according to following well-known Equation 1.⁴¹

$$C_{eq} = C \% + [(Si \% + P \%)/3] \quad \text{Eqn. 1}$$

It is a known fact that type and amount of trace elements that come from both charge materials and inoculants affect the microstructural features, like graphite morphology and mechanical properties, thus they should be controlled during casting.⁴¹⁻⁴⁵ As can be seen in Table 1, Mg contents of the novel cast irons are relatively higher than the range suggested (0.04–0.06 wt.%) for effective spheroidization of ductile cast irons. This is due to the difficulties in small size casting in laboratory practice and also due to the inconsistency in the composition of the charge material received and the datasheet provided by the supplier. Nevertheless, Mg content of the novel cast iron compositions are in the same range and will have similar effect on microstructural features. Due to the chemical compositions of the charge materials the P and S contents of the cast irons are higher than desired.

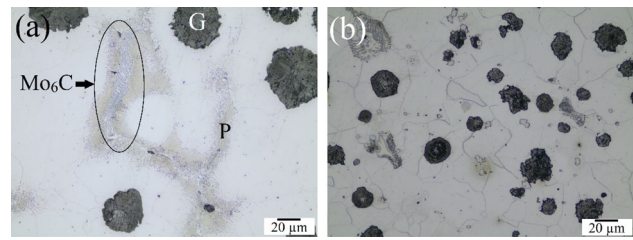


Figure 1. LM images showing the microstructures of the alloys; (a) SiMo and (b) SiNb.

Standard metallographic procedures are performed to determine the microstructural features of the cast alloys. The samples are etched by Nital (3 vol. % HNO_3) and microstructural characterization is carried out using both light microscope (LM, Olympus BX41M-LED), scanning electron microscope (SEM, Jeol JSM 6060) and energy-dispersive spectrometer (EDS, IXRF Systems Inc.).

The oxidation behavior of exhaust manifold materials is mostly studied under A_1 temperatures in order to simulate their working conditions and to avoid decarburization of austenite.³³⁻³⁶ Thus, initial stage oxidation is studied at 800 °C which is under the A_1 temperature of the alloys (850–960 °C), for 24 h, both in air and in a dry gas atmosphere (9 % CO_2 , 4 % O_2 and 87 % N_2) in furnace (MSA, Protherm). Although the selected gas atmosphere does not reflect the real combustion conditions, water vapor could not be included in the test conditions. Thus, the test atmosphere is defined as a dry gas atmosphere containing CO_2 and a flow rate of 12 mm.s^{-1} is utilized. The findings of oxidation tests are evaluated according to the atmospheres refereed as (i) air and (ii) dry gas. Samples are machined to form cylindrical geometry having a 12 mm \varnothing and 3 mm thickness and their flat surfaces are mirror-like polished for oxidation tests.

Following the furnace tests, no spallation is observed on the surfaces. Both flat surfaces and cross sections of the oxidized cast irons are characterized by 3D optical profilometer (Nanovea PS50), X-ray diffraction (XRD, Rigaku Ultima+) and SEM-EDS (Zeiss Evo10-IXRF) studies. XRD studies are carried out using $Cu-K\alpha$ radiation and a scanning speed of $1.0 \text{ }^\circ.\text{min}^{-1}$ is utilized.

Table 1. Chemical Compositions of the Cast Ductile Irons (wt.%)

Material	C	Si	Mo	Nb	Al	Mg	Mn	P	S	C_{eq}
SiMo	3.40	3.60	0.80	–	–	0.042	0.150	0.030	0.015	4.61
SiNb	3.57	4.04	–	0.96	0.02	0.074	0.231	0.057	0.028	4.93
SiNb-1Al	3.46	3.96	–	0.97	0.97	0.082	0.235	0.059	0.028	4.79
SiNb-2Al	3.47	3.99	–	1.03	2.03	0.078	0.245	0.057	0.032	4.82
SiNb-3Al	3.52	4.07	–	1.02	3.05	0.081	0.225	0.058	0.028	4.90
SiNb-4Al	3.54	4.05	–	1.04	4.03	0.079	0.228	0.055	0.035	4.91

Table 2. Amounts of Phases (Area %), Graphite Nodule Count and Nodularity (%) Determined by Image Analyses.

Material	Graphite	Carbide	Pearlite	Graphite nodule count/ mm ²	Graphite nodularity
SiMo	6.49 ± 0.17	0.72 ± 0.01	9.70 ± 0.27	466.74	88.21
SiNb	7.30 ± 0.30	1.13 ± 0.04	0.05 ± 0.01	452.35	82.26
SiNb-1Al	6.70 ± 0.40	1.08 ± 0.04	–	432.69	78.89
SiNb-2Al	6.20 ± 0.20	0.95 ± 0.02	–	240.04	76.84
SiNb-3Al	5.80 ± 0.20	0.89 ± 0.04	–	160.47	68.79
SiNb-4Al	5.20 ± 0.30	1.03 ± 0.03	–	149.50	71.74

Results and Discussion

Microstructure of the Alloys

Commercial SiMo ductile iron has nodular graphite (G), Mo-rich carbide (Mo₆C) and pearlitic areas (P) in a ferritic matrix (Figure 1a). In this alloy, which is used as exhaust manifold material, each microstructural feature is responsible for the required properties. Nodular graphite provides some desirable mechanical (high ductility and toughness) and physical (low thermal expansion) properties.^{46,47} Solid solution hardening of ferrite by silicon and dispersion hardening by Mo-rich carbides are responsible for the mechanical requirements.^{48–53} However, the presence of pearlite which forms as a result of inverse silicon segregation is undesirable due to its detrimental effect on the mechanical properties.^{14,35} In SiNb cast iron, similar matrix components like ferrite, nodular graphite, carbides and pearlite are present (Figure 1b). Although aluminum addition to the SiNb cast iron also results in a similar microstructure where graphite and carbides are embedded in the ferritic matrix (Figure 2), main difference is the absence of pearlitic areas. The absence of pearlite can be attributed to the change in segregation behavior of silicon by the presence of aluminum. It is a fact that alloying with

silicon retards the formation of grain boundary cementite. Aluminum is the other alloying element that has negligible solubility in cementite like silicon. Due to the segregation of aluminum around the graphite and segregation of silicon to the cell boundary, silicon is the responsible element for retardation of cementite precipitation.⁵⁴ The dissolution of aluminum in iron also causes silicon to accumulate at the cell boundaries in the solidified structure, thus preventing its inverse segregation and formation of pearlite.^{33,55–57} On the other hand, aluminum addition affects the amount and morphology of graphite as well. Microstructural investigations have revealed that the sphericity of graphite in the solidified structure decreases. This is due to the aluminum segregation around the graphite nodule, preventing carbon diffusion toward graphite and causing smaller graphite with vermicular morphology.^{20,55,58} Image analyses studies have been carried out on the cast irons to determine the amounts of phases stable at room temperature and the results are listed in Table 2. Although amount and nodularity of graphite within SiNb cast iron are similar as of SiMo ductile iron, pearlitic structure is much less due to the presence of the higher silicon content in the composition. Table 2 also shows the decrease in the amount of nodular graphite by increasing aluminum content. In our earlier studies on SiNb-xAl cast irons the quantities of various graphite morphologies (shape III, V and VI) present in the solidified structure have to be determined. It has been observed that as aluminum content of the alloy increased the nodularity of graphite decreased and the amount of graphite morphologies that cannot be classified increased as well.³⁵ In that case, the number of countable graphite decreases and due to the silicon segregation pearlite formation is suppressed.

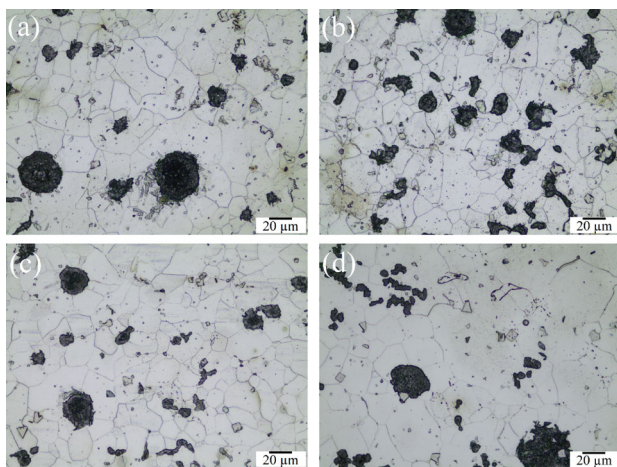


Figure 2. LM images showing the microstructures of the alloys; (a) SiNb-1Al, (b) SiNb-2Al, (c) SiNb-3Al and (d) SiNb-4Al.

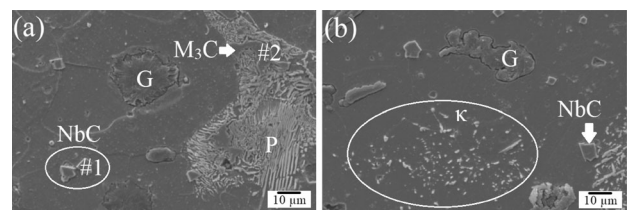


Figure 3. SEM images showing the microstructures of the alloys; (a) SiNb and (b) SiNb-4Al.

In Figure 3, SEM images for SiNb and SiNb-4Al alloys are given. In the solidified structure of SiNb alloy, carbide, pearlite and graphite are observed in the ferritic matrix (Figure 2a). Due to the presence of Nb as carbide former, Nb-rich carbides with faceted morphology are expected to form during solidification from liquid.^{33,35} The composition (Nb 94 : C 6 wt.%) attained by EDS analyses taken from point #1 in Figure 3a indicates the presence of NbC carbide. As it is well known, solidification of hyper eutectic cast irons produces cellular structure and positive and negative segregation of the elements take place at the liquid–solid interface (cell boundary).^{59,60} Due to the negative segregation of silicon, pearlitic regions at cell boundaries are expected⁵⁹ and are observed in the studied alloy as shown in Figure 3a. On the other hand, the positive segregation of carbide forming elements may cause the formation of eutectic carbides at the cell boundaries.^{61,62} Such a formation is observed at point #2 in Figure 3a, as M₃C type carbide with a composition (19.17 wt.% C, 77.70 wt.% Fe, 0.99 wt.% Si, 0.94 wt.% C, 1.20 wt.% Cr) determined by EDS. The microstructure of SiNb-4Al alloy, shown in Figure 3b, has aluminum rich precipitates in addition to NbC carbides. During crystallization of cast irons having aluminum above 4 wt.%, such precipitates are observed known as kappa (κ) phase.^{57,63}

Characterization of the Oxidized Alloys in Air Atmosphere

The oxidized surfaces of cast irons are composed of inner and outer layers. The inner oxide layer is formed by the outward diffusion of iron and the outer layer is formed due to the inward diffusion of oxygen.^{23,24} In the inner layer, oxides rich in Fe and Si are observed (FeO, Fe₂SiO₄, SiO₂, etc.) and in the outer layer mainly Fe₂O₃ and Fe₃O₄ exist. During the growth of outer oxide layer on the surface, phases like graphite and carbides present in the matrix are oxidized.²⁴ The surface characterization reveals the properties of outer oxide layer. Optical profilometer and SEM/

EDS studies are carried out on the surfaces and SEM/EDS is used to characterize the cross sections of the oxidized samples. The characteristic features of the outer oxide layer (oxide nodules, oxide layer and oxidized secondary phases) are examined by surface examination and features of the inner oxide layer are determined using cross sections of the oxidized samples.

In Figure 4, optical profilometer images of oxidized surfaces of SiMo and SiNb alloys are given. These images provide information about the width, height, amount, and distribution of the nodules on the surface.²⁴ The metal surface of SiMo alloy (Figure 4a), indicated by dark blue color (level 0 on z-axis), has a thin oxide layer (20-30 μm in height) on which nodules are present. These nodules are 200-250 μm in diameter and about 65 μm in height and have a tendency to expand and merge. This surface topography indicates a layered oxide scale. These findings are in agreement with those observed by Lekakh *et al.* (2020) in their study on the oxidation of SiMo alloy at elevated temperature. They have reported the presence of a rough oxide layer (7.5 μm) and coarse oxide nodules (300–700 μm) on the surface of the oxidized SiMo alloy.²⁴ On the other hand, the surface of SiNb alloy is covered with a 10 μm thick oxide layer on which nodules having 100–150 μm diameter and about 40 μm in height are present (Figure 4b). In this topography, the nodules are densely distributed and have not expanded and merged, yet. This indicates that SiNb alloy has better oxidation resistance provided by its higher silicon content. Effective Si-rich oxide formation in the inner layer slows down the formation of Fe-rich oxide nodules which are mainly responsible for the oxidation.^{23,24} These Fe-rich oxide nodules can form by two different mechanisms. In one of these mechanisms nodules grow simply by the expansion of the iron oxides at the initial stage of the oxidation. In the second mechanism on the other hand, the thin protective layer fractures locally and oxidizing gases penetrate

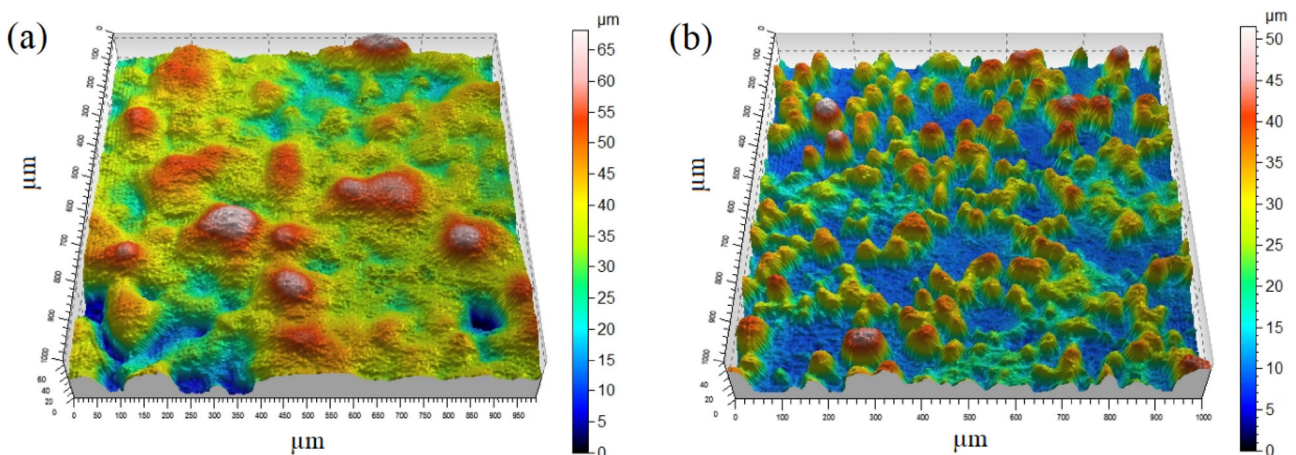


Figure 4. 3D images showing the surface morphology of the oxidized alloys; (a) SiMo and (b) SiNb.

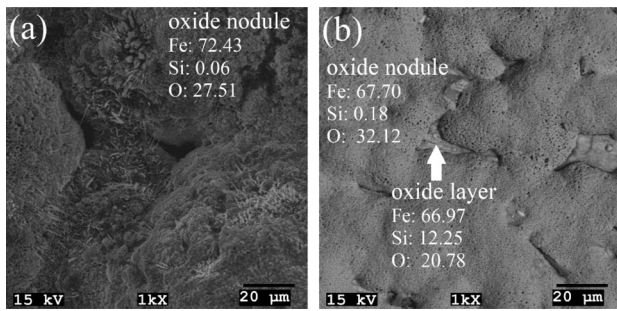


Figure 5. SEM images showing the surface morphology of the oxidized alloys; (a) SiMo and (b) SiNb.

through the subsurface defects causing nucleation and growth of the nodules under the failed protective layer.⁶⁴

SEM/EDS examinations have revealed the characteristics and chemical composition of the oxidized surfaces of SiMo and SiNb alloys (Figure 5). EDS data (wt.%) given in these figures show that both of these surfaces consist of typical Fe-rich oxide nodules that grow on Fe-Si-O layers. Fe-rich oxide nodules form at the beginning of the oxidation and as the oxidation progresses the outer Fe-rich oxide layer appears due to the tendency of growth and expansion of these nodules.⁶⁵ While the oxide layer covers the metal

surface, the diffusion of oxidizing agents decreases and oxidation rate of the metal decreases.⁵⁵

Figure 6 shows the 3D images of the SiNb-*x*Al alloys, and the effect of aluminum addition can be seen clearly as the following findings; (i) oxide layer gets thinner and at the highest aluminum content the original surface topography of the alloy (SiNb-4Al) appears, (ii) both distribution and amount of nodules decrease, (iii) tendency of growth of the nodules to outer surface decreases. All these findings indicate that by aluminum addition the formation of Fe-rich oxides is effectively inhibited.^{26,66} The decrease in oxidation kinetics of the alloy having the highest aluminum content is clearly seen by the distribution of small oxide nodules and slower growth of the oxide layer on the surface. In a study on the oxidation behavior of SiMo3Al alloy, Lekakh *et al.* (2020) have reported that by the aluminum addition, the oxide nodules get smaller and are distributed independently from each other on the oxidized metal surface. The aluminum addition causes the formation of an Al-rich oxide layer on the surface which inhibits the growth of oxide nodules resulting in a low surface roughness (2.5μm).²⁴

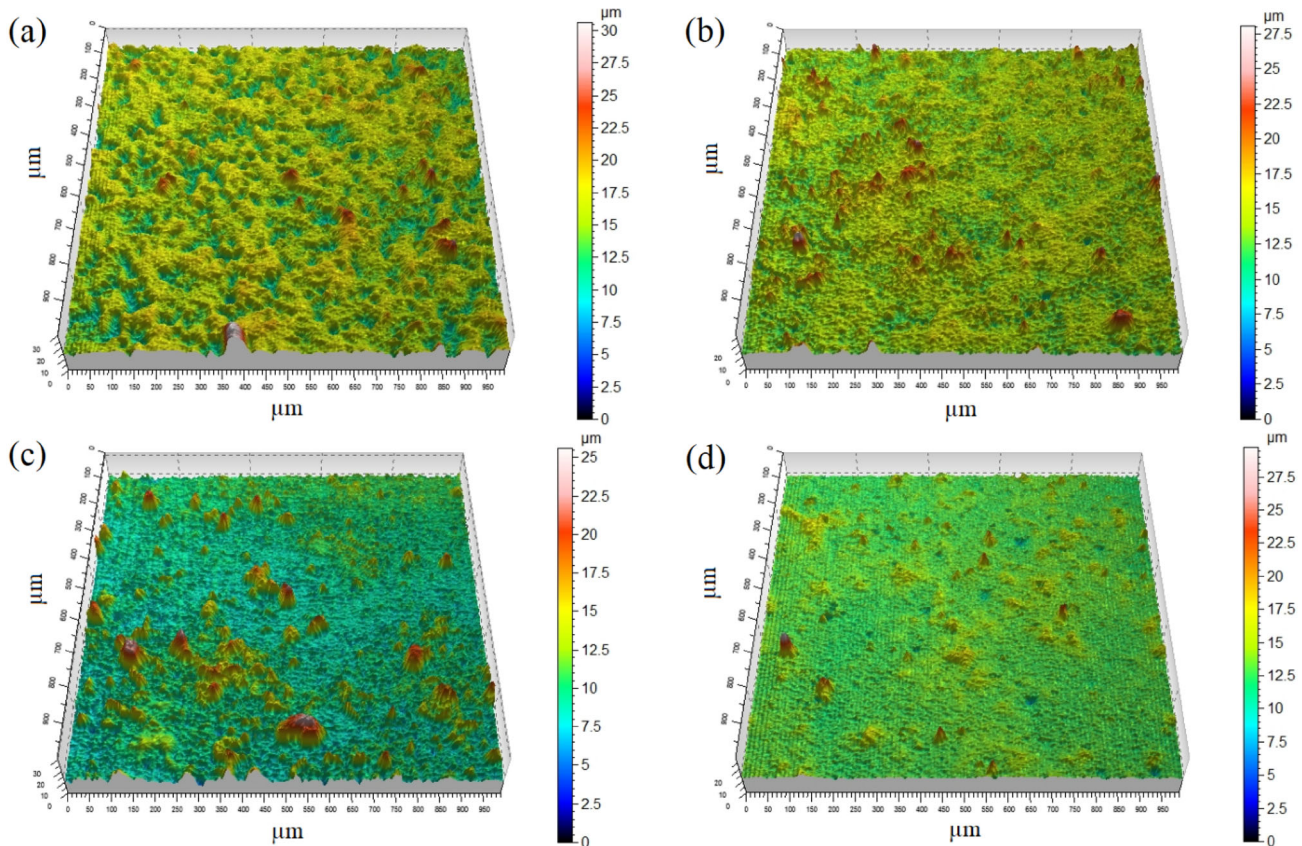


Figure 6. 3D images showing the surface morphology of the oxidized alloys; (a) SiNb-1Al, (b) SiNb-2Al, (c) SiNb-3Al and (d) SiNb-4Al.

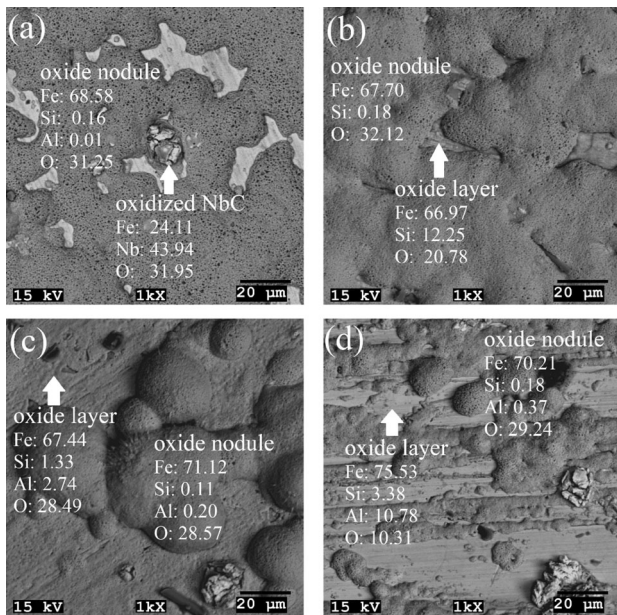


Figure 7. SEM images showing the surface morphology of the oxidized alloys; (a) SiNb-1Al, (b) SiNb-2Al, (c) SiNb-3Al and (d) SiNb-4Al.

SEM/EDS studies on the oxidized surfaces of SiNb-*x*Al alloys reveal the presence of aluminum within the iron rich oxide forms (Figure 7a-d). This is due to the presence of Al-rich oxides (AlFeO₃ or Al₂O₃) present in the inner oxide layer in aluminum-modified cast iron compositions.^{24,26,27,36} The presence of Al-rich oxides in oxide layer causes the decreased expansion of Fe-rich oxide nodules resulting in a slower growth of the oxide layer on the surface. As it is well known, aluminum rich oxides prevent the inward diffusion of the oxidizing agents thus causing slower oxidation kinetics.⁶⁶⁻⁶⁸ Due to this slower growth, the oxide layer cannot cover the whole surface as a result of which the oxidation of NbC in the ferritic matrix has been observed clearly (Figure 7a-d). On the other hand, nodules can grow after the nucleation of a thin protective oxide layer on the metal surface. It is unavoidable that thin protective oxide layer cracks and oxidizing gas agents progress through the defects under the oxide layer and contribute to the growth of nodules.⁶⁵ The SEM image given in Figure 7c shows the smooth oxide layer covering the surface and the nodules that grow and coalesce on it. Ibrahim *et al.*²⁶ have reported that the amount of aluminum addition alters both oxide components and layer thicknesses. At low aluminum addition, a thick oxide layer rich in iron oxide forms and as the aluminum content increases, AlFeO₃ starts to form resulting in a decrease in the layer thickness. Further increase in aluminum provides a thin, stable Al₂O₃ in the oxide layer inhibiting the formation of iron oxides.²⁶ As it is well known, the protective oxide layers like Cr₂O₃, Al₂O₃ act as barriers to the diffusion of oxygen and iron ions as a result which growth of iron oxide layers can be reduced.^{19,20,23,26,69}

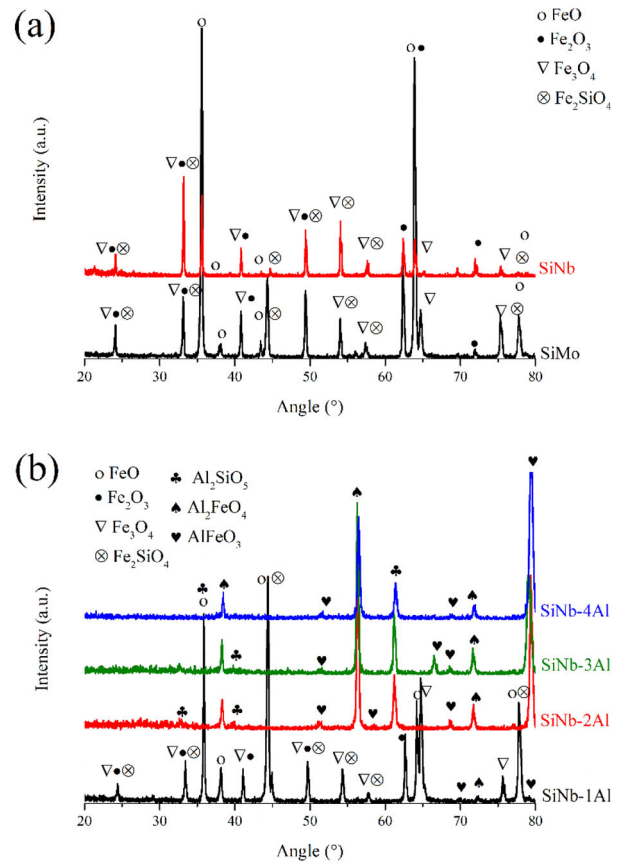


Figure 8. XRD patterns of (a) SiMo and SiNb and (b) SiNb-*x*Al alloys the oxidized at 800 °C.

The oxides formed on the surfaces of the SiMo and SiNb alloys are characterized by XRD and the diffractograms are given in Figure 8. SiMo and SiNb alloys have iron and iron-silicon oxides like FeO, Fe₂O₃, Fe₃O₄ and Fe₂SiO₄ on their surfaces (Figure 8a). Studies have shown that inner layer consists of FeO and Si-rich Fe₂SiO₄ / SiO₂ oxides^{38,65} while the outer layer has Fe₃O₄ and Fe₂O₃ oxides.^{23,69} The XRD data of SiNb-*x*Al alloys are given in Figure 8b and iron and iron-silicon oxides (FeO, Fe₂O₃, Fe₃O₄ and Fe₂SiO₄) are detected on their surfaces. The decrease in the intensity of ferrous oxides can be attributed to the presence of Al-rich oxides (Al₂SiO₅, Al₂FeO₄ and AlFeO₃) which are responsible for the decrease in outward diffusion of iron and inward diffusion of oxygen.

LM images showing the cross sections of the oxidized SiMo and SiNb alloys are given in Figure 9. The difference in the silicon content of the alloys determines the thickness of the oxide layer formed during oxidation. SiNb alloy having higher Si content has a thinner layer compared to SiMo alloy. Despite the difference in thickness of the oxide layers, both alloys have inner and outer oxide layers having voids, visible in distinctive contrasts. The cross section observations confirm the surface examinations that a smooth layer is formed on the surface of SiMo alloy due to

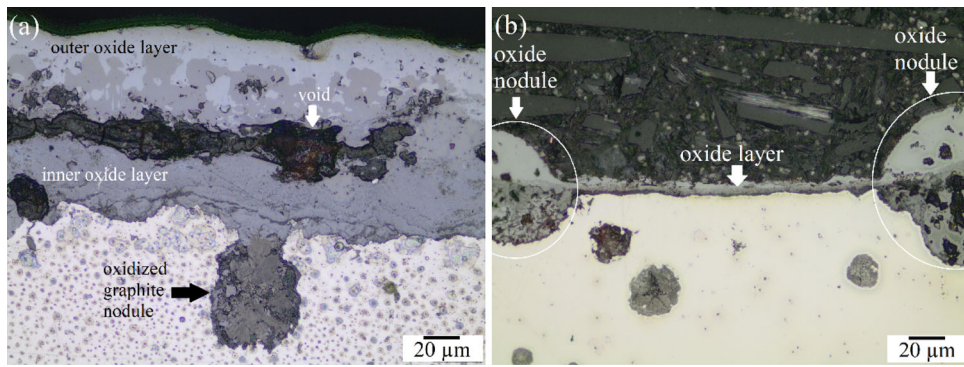


Figure 9. LM images showing the cross sections of oxidized SiMo (a) and SiNb (b) alloys tested at 800 °C.

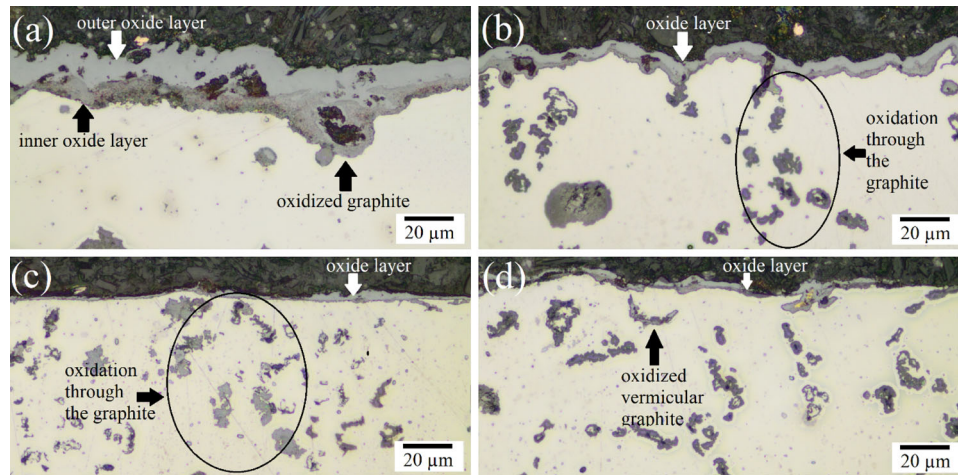


Figure 10. LM images showing the cross sections of the alloys oxidized at 800 °C for 24 h; (a) SiNb-1Al, (b) SiNb-2Al, (c) SiNb-3Al and (d) SiNb-4Al.

the merging of the nodules and oxidation progresses through the oxide nodules on the surface of SiNb alloy.

Figure 10 shows LM images of the cross sections of oxidized aluminum-modified SiNb alloys. The decrease in the thickness of oxide layer as aluminum addition increases can be clearly followed. This is due to the formation of protective Al-rich oxides ($\text{AlFeO}_4/\text{Al}_2\text{O}_3$) having a barrier effect toward the diffusion of oxidizing agents like iron and oxygen ions.^{66–68} The examinations on the cross sections of the oxidized alloys reveal that the oxide scale consists of inner and outer layers and the oxidation progresses by the growth of the oxide layer and coalescence of the oxide nodules as discussed in the surface characterization. As can be seen from Figure 10, the graphite morphology also affects the oxidation behavior of Al-modified alloys since oxidizing agents can diffuse more easily toward the matrix through vermicular graphite. As it is well known, aluminum segregates around the graphite nodule and inhibits carbon diffusion toward graphite during solidification. Thus, aluminum causes a decrease in graphite size and changes its morphology resulting in increased vermicular graphite^{55,70} Oxidation of vermicular graphite also causes

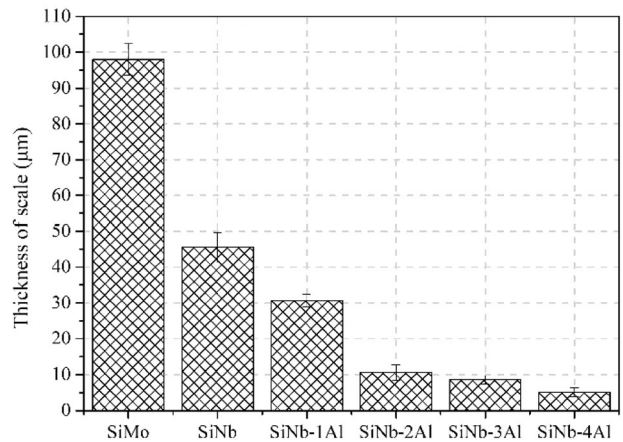


Figure 11. The thickness variation of the oxide layers on SiMo and SiNb-xAl alloys tested in air atmosphere.

the formation of voids due to decarburization.²⁴ In a recent study on the effect of microstructural features on the oxidation behavior of SiMo cast iron, the change in graphite morphology by aluminum addition has been studied using μCT imaging. It is observed that oxidation and decarburization progress through the interface of graphite that loses

its nodularity. Thus, increase in aluminum content causes higher amount of vermicular graphite resulting in increased oxidation and decarburization toward the matrix. This is due to the disruption (like formation of a void) between the graphite nodule and the metal surface, as a result of which free pass is provided for oxygen.^{31,71}

During the cross section studies the oxide scale thicknesses of SiMo and SiNb-xAl cast irons tested in air atmosphere are measured and shown in Figure 11. Surface investigations have revealed the presence of a dense and expanded oxide layer on the surface of SiMo cast iron compared to SiNb cast iron. Therefore, it is inevitable that the thickness of oxide scale on SiMo cast iron (98 μm) is higher than that of SiNb cast iron (45 μm). Such a thick oxide layer is also observed by Lekakh *et al.* (2020) on the surface of SiMo cast iron, and it is reported that after oxidation at 650-800 °C for 100 hours, 100-150 μm thick oxide layer can form.²⁴ As aluminum is added to SiNb cast iron, due to the formation of protective Al-rich oxides the thicknesses of oxide scales on SiNb-xAl can be reduced as observed in Figure 11. Considering the thicknesses of oxide scales formed during oxidation tests in air atmosphere, for the highest aluminum addition the thickness is decreased about 95 % and 90 % compared to SiMo and SiNb cast irons, respectively. Effect of aluminum on the reduction in oxide layer thickness is reported earlier for SiMo3Al cast iron that is oxidized at 650-800 °C for 100 hours. The formation of an oxide layer only 5-15 μm thick, at all test temperatures, is attributed to the formation of Al-rich oxide layer.²⁴ Lekakh *et al.* in their microtopographic studies (μCT) on oxidation of SiMo1.8Al ve SiMo3Al cast irons have reported that an alumina film forms between the scale and metal matrix which provides resistance to both oxidation and decarburization.³¹ Ibrahim *et al.* have a similar observation for a SiMo cast iron having 3 % Al. Cyclic oxidation tests carried out at 900 °C for 600 hours have revealed that a thinner oxide layer is formed on the surface of the alloy compared to the one that does not have any aluminum addition.²⁰

Characterization of the Oxidized Alloys in Dry Gas Atmosphere

The surfaces of the SiMo and SiNb alloys oxidized under dry gas atmosphere containing CO_2 are examined by optical profilometer and the obtained 3D images are given in Figure 12. As shown in Figure 12a, an oxide layer of 15-20 μm thick covers the surface of SiMo alloy, nodules are present about 100 μm in width and 35-40 μm in height on the oxidized surface, most of which have combined and expanded. A thinner oxide layer (5-10 μm) is observed on the surface of SiNb alloy and nodules having 50 μm width and 30-35 μm height are present on the surface (Figure 12b) due to higher silicon content which provides a Si-rich oxide layer acting as a better oxidation barrier.^{36,65} Smaller oxide nodules are observed in both alloys compared to oxidation in air atmosphere due to the lower oxygen content in exhaust gas atmosphere.

SEM images showing the oxidized surfaces of SiMo and SiNb alloys tested at 800 °C in gas atmosphere are given in Figure 13. A continuous Fe and Si rich oxide layer covers the whole surface and needle shaped Fe-rich oxide nodules primarily growing on graphite are observed as seen in Figure 13a. This is a typical oxide formation in SiMo alloys as observed in earlier studies.^{19,23,24} Oxidation tests at 850 °C in gas atmospheres having compositions, 5% CO_2 +12% O_2 +83% N_2 and 10% CO_2 +12% O_2 +78% N_2 have shown that oxides like Fe_2O_3 , Fe_3O_4 and SiO_2 may form on the surface of SiMo cast iron.⁷²

Similar features are observed on the oxidized surface of the SiNb alloy (Figure 13b). A continuous Fe-Si oxide layer covers the surface and spongy iron oxide nodules are seen on this layer.

The effect of aluminum addition can be seen in 3D images of the SiNb-xAl alloys given in Figure 14. Although findings are similar to those observed in air atmosphere, the oxide layer is thinner and as aluminum addition increases

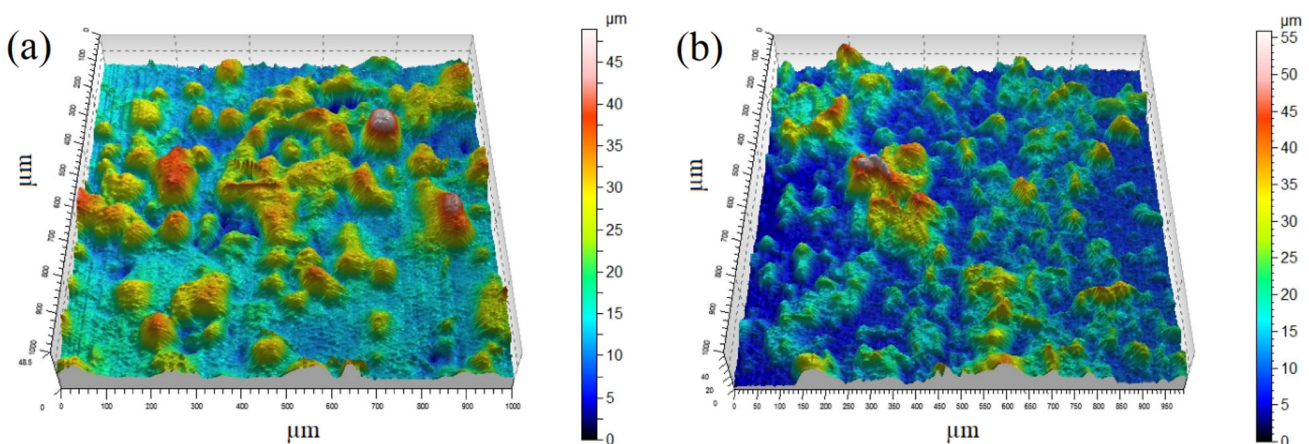


Figure 12. 3D images showing the surface morphology of the oxidized alloys; (a) SiMo and (b) SiNb.

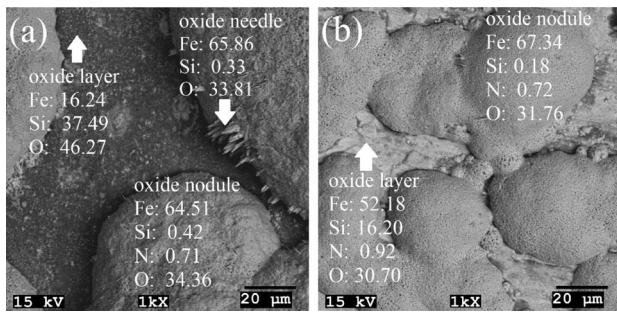


Figure 13. SEM images showing the surface morphology of the oxidized alloys; (a) SiMo and (b) SiNb.

the topography of the metal surface can be observed clearly. Even though surface topography forms due to the oxidation of graphite rather than ferritic matrix, ΔZ which reflects the difference between the surface and top of deposited oxide does not increase since Al-rich oxides having protective effect form around the graphite and prevent the growth of oxide nodules. As a result, the amount of oxide nodules decreases as aluminum increases. These results are verified by SEM examinations given in Figure 15. A thin Al-rich oxide layer covers the whole surface of the alloys, as aluminum addition increases further, amount and size of spongy iron oxide nodules decrease (Figure 15). This is due to the thermodynamic

priority of Al-rich oxide formation.²⁶ Oxidation tests performed by Chandra-Ambhorn *et al.* in CO₂ containing atmospheres have revealed that the oxidation resistance of SiMo cast iron increases with 5.45 wt. % Al addition, due to the formation of alumina layer on the surface.⁷²

During oxidation in gas atmosphere, a rapid formation of Al-rich oxide layer occurs and grows as multilayer structure is depleted in aluminum content. This phenomenon is clearly detected by EDS point analyses as labeled on Figure 15b and obtained data is given in Table 3. According to the elemental compositions, the metal surface is covered by oxide layer having the highest aluminum content (Figure 15b, #1). As oxidation progresses, diffusion of iron contributes to the growth of oxide layer and multilayered structure forms accompanied by a decrease in aluminum content (Figure 15b, #2–5).

The findings on the surface studies are supported by EDS analyses on the cross sections of SiNb and SiNb-4Al alloys as given in Figures 16 and 17. As seen in Figure 16a, although fractured oxide layers exist due to the difference in expansion coefficients of metal substrate and oxide layers,²³ the cross section structure consists of oxidized graphite and carbides. The EDS data taken from the cross section of SiNb alloy indicate that the top layer

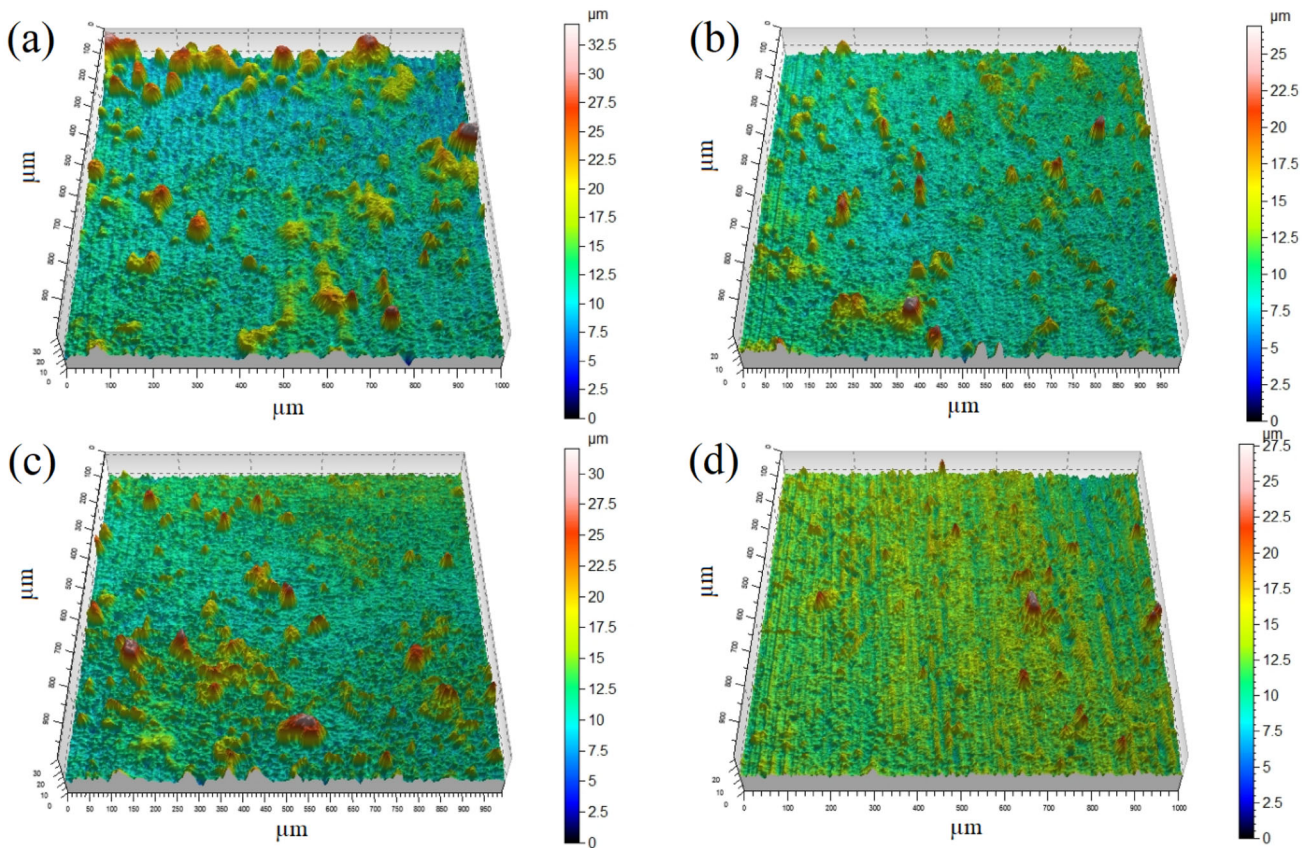


Figure 14. Optical profilometer images showing the surface morphology of the oxidized alloys; (a) SiNb-1Al, (b) SiNb-2Al, (c) SiNb-3Al and (d) SiNb-4Al.

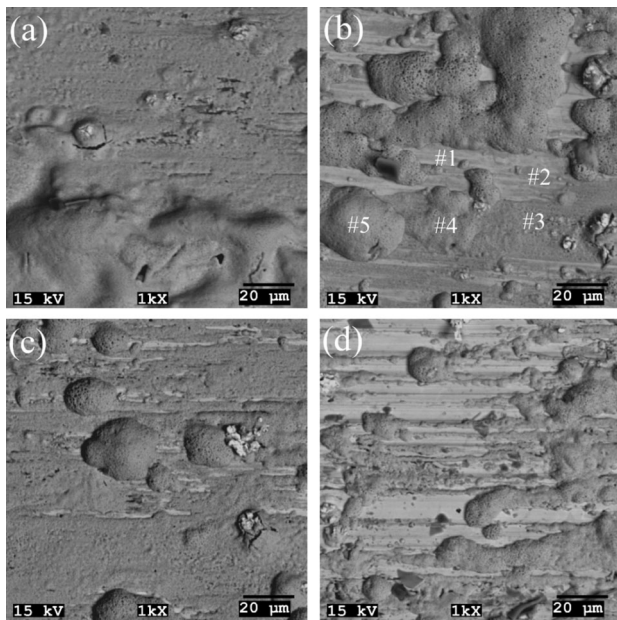


Figure 15. SEM images showing the surface morphology of the oxidized alloys; (a) SiNb-1Al, (b) SiNb-2Al, (c) SiNb-3Al and (d) SiNb-4Al.

Table 3. EDS Data (wt.%) Obtained from the Oxidized Surface of SiNb-2Al Alloy

Point	Al	Si	Fe	N	O
#1	9.99	4.20	73.80	0.79	11.22
#2	9.67	4.12	60.46	0.67	25.08
#3	8.11	4.27	63.79	0.71	23.01
#4	3.79	2.10	62.55	0.89	30.65
#5	0.65	0.23	61.85	0.62	36.64

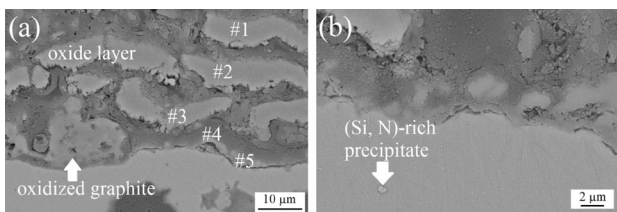


Figure 16. SEM images showing the cross sections of the oxidized SiNb alloy; (a) oxide layer and (b) precipitate in the matrix.

(Figure 16a, #1) is formed by Fe-rich oxides and toward the matrix (Figure 16a, #2-5), the amount of silicon increases while iron decreases (Table 4). This result proves that the outer oxide layer consists of Fe_2O_3 and Fe_3O_4 while the inner layer is formed by FeO , Fe_2SiO_4/SiO_2 . The nitrogen amount is highest at interface of metal substrate and oxide layer (Figure 16a, #5). During the oxidation tests of cast irons in exhaust gas atmosphere, Tholence and Norell have reported that a nitride zone is formed and Si_3N_4

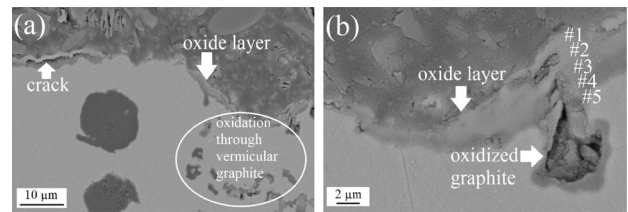


Figure 17. SEM images showing the cross sections of the oxidized SiNb-4Al alloy; (a) oxide layer and (b) oxidized graphite.

precipitates exist in the ferritic matrix as well as $MgSiN_2$ precipitates are present at the eutectic cell boundaries.^{18,19} In SiNb alloy, a similar phenomenon is observed since precipitates rich in silicon and nitrogen (52 Fe wt.%, 30 Si wt.%, 18 N wt.%) are present in the matrix as seen in Figure 16b. In order to investigate the effect of aluminum addition to the oxidation behavior, cross section of SiNb-4Al oxidized in exhaust gas atmosphere is examined by SEM/EDS analyses (Figure 17). The thin oxide layer formed on the metal surface has heterogeneous thickness and spallation and cracks are observed at some areas. Besides, it can be clearly seen that oxidation progresses from surface toward the matrix through vermicular graphite network (Figure 17a). EDS data taken from the points labeled in Figure 17b are given in Table 4 and reveal that the top of oxide layer consists of Fe-rich oxides (Figure 17b, #1) and toward the matrix both aluminum and silicon content increase (Figure 17b, #2-5) proving the presence of the protective Si and Al-rich oxides like Fe_2SiO_4/SiO_2 , $AlFeO_3/Al_2O_3$. According to the data, it can be concluded that the barrier effect is mainly due to the formation of Al-rich oxides rather than Si-rich oxides and similar to SiNb alloy, due to presence of N_2 in the exhaust gas, the nitrogen level also increases toward the matrix having high nitrogen solubility (Table 4).

Figure 18 indicates the oxide scale thicknesses of SiMo and SiNb-xAl cast irons tested in dry gas atmosphere. Even

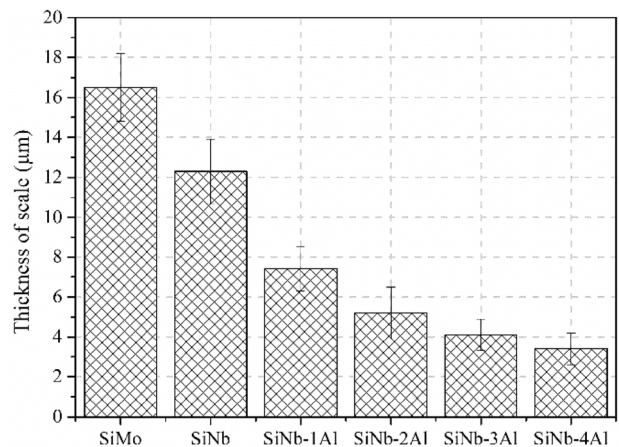


Figure 18. The thickness variation of the oxide layers on SiMo and SiNb-xAl alloys tested in dry gas atmosphere.

Table 4. EDS data (wt.%) obtained from the cross sections of oxidized SiNb and SiNb-4Al alloys.

Point	SiNb Si	SiNb-4Al Fe	O	N	Si	Fe	Al	O	N
#1	0.87	93.89	2.47	0.03	1.53	87.29	1.74	3.20	0.01
#2	1.18	90.21	3.71	0.24	2.26	80.74	8.76	2.48	0.11
#3	10.98	70.92	4.88	0.43	8.23	67.82	13.90	5.59	0.43
#4	11.54	68.86	5.76	1.35	7.66	66.15	16.97	5.10	0.76
#5	16.12	64.17	7.49	1.68	12.47	48.94	24.56	9.88	2.26

though the thicknesses of oxide scale are less than those in air atmosphere (Figure 11) due to the lower O₂ content in dry gas atmosphere, similar trend is observed: (i) SiMo cast iron has the thickest oxide scale (16.5 μm) compared to the SiNb-xAl cast irons and (ii) aluminum addition to the SiNb cast iron reduces the thicknesses of the oxide scales.

The presence of all oxides formed on the surfaces of all the alloys tested in gas atmosphere at 800 °C is verified by

XRD analyses as shown in Figure 19. As similar to the findings obtained from air oxidation studies, SiMo and SiNb alloys have Fe and Si rich oxides (Fe₂O₃, Fe₃O₄, FeO and Fe₂SiO₄), whereas in SiNb-xAl alloys, Al-rich oxides (Al₂FeO₄, AlFeO₃ and Al₂SiO₅) are detected as well. The intensities of the Fe-rich oxide peaks decrease as Al-rich oxide peaks appear.

Conclusion

In this study, initial stage oxidation of novel SiNb-xAl (x:0-4 wt.%) ductile cast iron compositions to be used as potential exhaust manifold materials are evaluated in air and CO₂-containing gas atmospheres. Oxidation tests revealed that multi-layered and porous oxide scales formed and spongy oxide nodules grew on the metal surface. The oxidized surfaces of SiMo and SiNb alloys had spongy Fe-rich oxide nodules (Fe₂O₃, Fe₃O₄, FeO) on a smooth Si-rich oxide scale (Fe₂SiO₄/SiO₂). Although the surface characteristics of oxidized alloys were similar at both atmospheres, due to the lower oxygen content in gas atmosphere, thinner oxide layers and dispersed smaller nodules were observed. As aluminum was added to SiNb alloy, spongy Fe-rich oxides became smaller and got lesser compared to SiNb and the surface was covered by thinner Al-rich oxide scale (Al₂SiO₅, Al₂FeO₄ and AlFeO₃). Thus, SiNb-xAl alloys can be suggested as alternative exhaust manifold materials at elevated temperatures due to their better oxidation resistance.

Acknowledgement

The authors, G. AktaşÇelik, Ş Polat and Ş H. Atapek, wish to acknowledge the financial support given by Scientific Research Projects Coordination Unit of Kocaeli University under the project numbers 2017/118 and 2019/118.

REFERENCES

1. A.A. Partoaa, M. Abdolzadeh, M. Rezaeizadeh, Effect of fin attachment on thermal stress reduction of

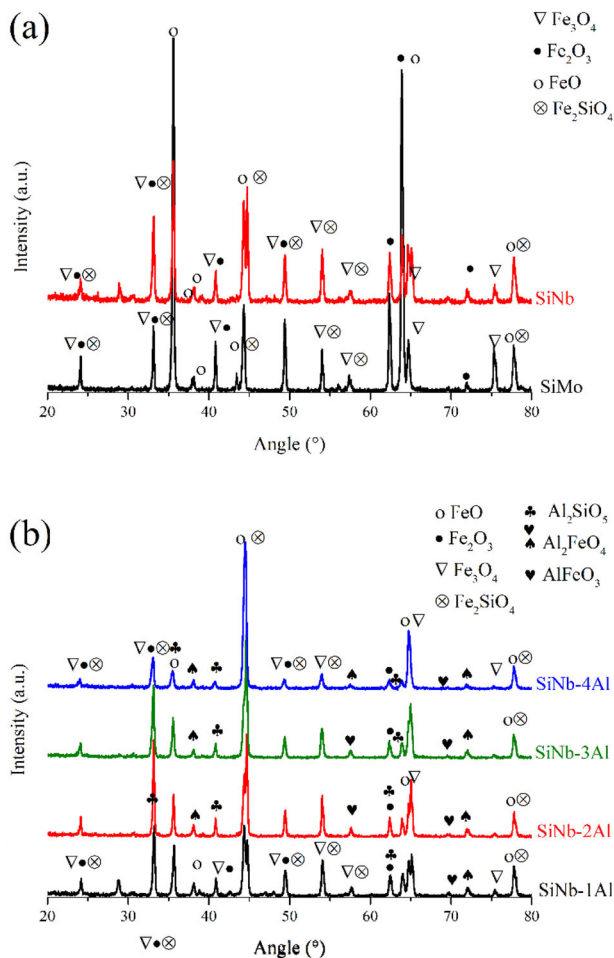


Figure 19. XRD patterns of (a) SiMo and SiNb and (b) SiNb-xAl alloys the oxidized at gas atmosphere at 800 °C.

- exhaust manifold of an off road diesel engine. *J. Cent. South. Univ.* **24**, 546–559 (2017). <https://doi.org/10.1007/s11771-017-3457-1>
2. T. Johnson, A., Joshi, review of vehicle engine efficiency and emissions. *SAE Int. J. Eng.* **11**(6), 1307–1330 (2018)
 3. M. Ekström, S. Jonsson, High-temperature mechanical-and fatigue properties of cast alloys intended for use in exhaust manifolds. *Mater. Sci. Eng. A* **616**, 78–87 (2014). <https://doi.org/10.1016/j.msea.2014.08.014>
 4. L.M. Åberg, C. Hartung, Solidification of SiMo nodular cast iron for high temperature applications. *Trans. of Indian Inst. Met.* **65**, 633–636 (2012). <https://doi.org/10.1007/s12666-012-0216-8>
 5. J.P. Shingledecker, P.J. Maziasz, N.D. Evans, M.J. Pollard, Creep behavior of a new cast austenitic alloy. *Int. J. Press. Vessels Pip.* **84**, 21–28 (2007). <https://doi.org/10.1016/j.ijpvp.2006.09.014>
 6. H. Kazdal Zeytin, C. Kubilay, H. Aydın, A.A. Ebrinc, B. Aydemir, Effect of microstructure on exhaust manifold cracks produced from SiMo ductile iron. *J. Iron. Steel Res. Int.* **16**, 32–36 (2009). [https://doi.org/10.1016/S1006-706X\(09\)60040-6](https://doi.org/10.1016/S1006-706X(09)60040-6)
 7. P.J. Maziasz, Development of creep-resistant and oxidation-resistant austenitic stainless steels for high temperature applications. *JOM* **70**, 66–75 (2018). <https://doi.org/10.1007/s11837-017-2642-x>
 8. F. Tholence, M. Norell, High temperature corrosion of cast alloys in exhaust environments. II - cast stainless steels. *Oxid. Met.* **69**, 37–62 (2008). <https://doi.org/10.1007/s11085-007-9082-x>
 9. M.P. Brady, G. Muralidharan, D.N. Leonard, J.A. Haynes, R.G. Weldon, R.D. England, Long-term oxidation of candidate cast iron and stainless steel exhaust system alloys from 650 to 800 °C in air with water vapor. *Oxid. Met.* **82**, 359–381 (2014). <https://doi.org/10.1007/s11085-014-9496-1>
 10. Y.H. Zhang, M. Li, L.A. Godlewski, J.W. Zindel, Q. Feng, Effective design of new austenitic cast steels for ultra-high temperature automotive exhaust components through combined CALPHAD and experimental approaches. *Metall. and Mater. Trans. A* **47**, 3289–3294 (2016). <https://doi.org/10.1016/j.msea.2016.12.023>
 11. R. Osei, S. Lekakh, R. O'Malley, Effect of Al Additions on scale structure and oxidation kinetics of 430-ferritic stainless steel reheated in a combustion atmosphere. *Metall. and Mater. Trans. B* **52**, 3423–3438 (2021). <https://doi.org/10.1007/s11663-021-02272-w>
 12. P. Matteis, G. Scavino, A. Castello, D. Firrao, High temperature fatigue properties of a Si-Mo ductile cast iron. *Procedia Mater. Sci.* **3**, 2154–2159 (2014). <https://doi.org/10.1016/j.mspro.2014.06.349>
 13. P. Matteis, G. Scavino, A. Castello, D. Firrao, High-cycle fatigue resistance of Si-Mo ductile cast iron as affected by temperature and strain rate. *Metall. and Mater. Trans. A* **46**, 4086–4094 (2015). <https://doi.org/10.1007/s11661-015-3029-7>
 14. G.A. Çelik, M.I.T. Tzini, Ş Polat, J.S. Aristeidakis, ŞH. Atapek, P.I. Sarafolou, G.N. Haidemenopoulos, Simulation and analysis of the solidification characteristics of a Si-Mo ductile iron. *J. Min. Metall. Sect. B.* **57**, 53–62 (2021). <https://doi.org/10.2298/JMMB200717003C>
 15. Y. Li, J. Liu, W. Huang et al., Failure analysis of a diesel engine exhaust manifold. *Inter Metalcast* (2022). <https://doi.org/10.1007/s40962-022-00796-8>
 16. Ekström M. Oxidation and corrosion fatigue aspects of cast exhaust manifolds Ph.D. thesis KTH Royal Institute of Technology; 2015.
 17. D. Pierce, A. Haynes, J. Hughes, R. Graves, P. Maziasz, G. Muralidharan et al., High temperature materials for heavy duty diesel engines: historical and future trends. *Prog Mater Sci* **103**, 109–179 (2019). <https://doi.org/10.1016/j.pmatsci.2018.10.004>
 18. F. Tholence, M. Norell, Nitride precipitation during high temperature corrosion of ductile cast irons in synthetic exhaust gases. *J. Phys. Chem. Solids* **66**, 530–534 (2005). <https://doi.org/10.1016/j.jpcs.2004.05.010>
 19. F. Tholence, M. Norell, High temperature corrosion of cast alloys in exhaust environments. I – ductile cast irons. *Oxid. Met.* **69**, 13–36 (2008). <https://doi.org/10.1007/s11085-007-9081-y>
 20. M.M. Ibrahim, A. Nofal, M.M. Mourad, Microstructure and hot oxidation resistance of SiMo ductile cast irons containing Si-Mo-Al. *Metall. and Mater. Trans. B* **48**, 1149–1157 (2017). <https://doi.org/10.1007/s11663-016-0871-y>
 21. M. Stawarz, P.M. Nuckowski, Effect of Mo addition on the chemical corrosion process of SiMo cast iron. *Materials* **13**, 1745 (2020). <https://doi.org/10.3390/ma13071745>
 22. M. Stawarz, SiMo ductile iron crystallization process. *Arch. Foundry Eng.* **17**, 147–152 (2017). <https://doi.org/10.1515/afe-2017-0027>
 23. M. Ekström, P. Szakalos, S. Jonsson, Influence of Cr and Ni on high-temperature corrosion behavior of ferritic ductile cast iron in air and exhaust gases. *Oxid. Met.* **80**, 455–466 (2013). <https://doi.org/10.1007/s11085-013-9389-8>
 24. S.N. Lekakh, A. Bofah, W.-T. Chen, L. Godlewski, M. Li, Prevention of high-temperature surface degradation in SiMo Cast Irons by Cr and Al alloying. *Metall Mater Trans B* **51**, 2542–2554 (2020). <https://doi.org/10.1007/s11663-020-01975-w>
 25. C. Delprete, R. Sesana, Experimental characterization of a Si–Mo–Cr ductile cast iron. *Mater. Des.* **57**, 528–537 (2014). <https://doi.org/10.1016/j.matdes.2014.01.002>
 26. M.M. Ibrahim, M.M. Mourad, A.A. Nofal, A.I.Z. Farahat, Microstructure, hot oxidation resistance and damping capacity of Al- alloyed cast iron. *Int. J. Cast*

- Met. Res. **30**, 61–69 (2017). <https://doi.org/10.1080/13640461.2016.1239895>
27. S. Chandra-ambhorn, T. Tummaporn, P. Jiradech, High temperature oxidation of Al-alloyed SiMo cast iron in CO₂-containing atmospheres. *Adv. Mater. Res.* **813**, 132–135 (2013). <https://doi.org/10.4028/www.scientific.net/amr.813.132>
 28. S. Xiang, B. Zhu, S. Jonsson, High-temperature corrosion-fatigue behavior of ductile cast irons for exhaust manifolds applications. *Mater. Sci. Forum* **925**, 369–376 (2018). <https://doi.org/10.4028/www.scientific.net/MSF.925.369>
 29. N. Scheidhauer, C. Doöaschk, G. Wolf, Oxidation resistant cast iron for high temperature application. *Mater. Sci. Forum* **925**, 393–399 (2018). <https://doi.org/10.4028/www.scientific.net/MSF.925.393>
 30. H.K.D.H. Bhadeshia, R.W.K. Honeycombe, *Steels Microstructure and Properties*, 3rd edn. (Elsevier Ltd., Oxford, UK, 2006)
 31. S.N. Lekakh, C. Johnson, L. Godlewski et al., Control of high-temperature static and transient thermomechanical behavior of SiMo Ductile Iron by Al alloying. *Inter Metalcast* (2022). <https://doi.org/10.1007/s40962-022-00768-y>
 32. G. Aktaş Çelik, M-I. T. Tzini, Ş. H. Atapek, Ş. Polat, G. N. Haidemenopoulos, Computation of the effect of alloying elements on the physical properties of SiMo ductile cast iron. in *Proc. IMMC19*, (2018) 1086-1089.
 33. G. Aktaş Çelik, Egzoz manifoldu olarak kullanılan sünek dökme demirlerin alaşımlama ile geliştirilmesi, PhD Thesis, 2020, Kocaeli, Turkey.
 34. G. Aktaş Çelik, M.-I.T. Tzini, Ş.H. Atapek, Ş. Polat, G.N. Haidemenopoulos, Matrix design of a novel ductile cast iron modified by W and Al: a comparison between thermodynamic modeling and experimental data. *Metall. Mater. Eng.* **26**, 15–29 (2020). <https://doi.org/10.30544/449>
 35. G. Aktaş Çelik, M.-I.T. Tzini, Ş.H. Atapek, Ş. Polat, G.N. Haidemenopoulos, Thermal and microstructural characterization of a novel ductile cast iron modified by aluminum addition. *Int. J. Miner. Metall. Mater.* **27**, 190–199 (2020). <https://doi.org/10.1007/s12613-019-1876-8>
 36. G. Aktaş Çelik, Ş.H. Atapek, Ş. Polat, M-I.T. Tzini, G. N. Haidemenopoulos, Hot oxidation resistance of a novel cast iron modified by Nb and Al addition for exhaust manifold applications. *Metall. and Mater. Trans. A*, (2022), in press.
 37. A. Ebel, O. Marsan, J. Lacaze, B. Malard, Cyclic oxidation of high- silicon spheroidal graphiteiron. *Corros. Sci.* **192**, 109854 (2021). <https://doi.org/10.1016/j.corsci.2021.109854>
 38. A. Ebel, S.Y. Brou, B. Malard, J. Lacaze, D. Monceau, L. Vaissière, High-temperature oxidation of a high silicon SiMo spheroidal cast iron in air with in situ change in H₂O content. *Mater. Sci. Forum* **925**, 353–360 (2018). <https://doi.org/10.4028/www.scientific.net/msf.925.353>
 39. S.N. Lekakh, C. Johnson, A. Bofah et al., Improving high-temperature performance of high Si-alloyed ductile iron by altering additions. *Inter Metalcast* **15**, 874–888 (2021). <https://doi.org/10.1007/s40962-020-00524-0>
 40. K. Dawi, J. Favergeon, G. Moulin, High temperature corrosion of the Si-Mo cast iron in exhaust atmosphere. *Mater. Sci. Forum* **595–598**, 743–751 (2008). <https://doi.org/10.4028/www.scientific.net/MSF.595-598.743>
 41. ASM Handbook, Vol. 1, Properties and Selection: Irons, Steels, and High Performance Alloys, 4th ed., ASM International, Ohio, pp. 17-210, (1995).
 42. G. Alonso, D.M. Stefanescu, J. Sanchez et al., Effect of the type of inoculant on the shrinkage porosity of high-silicon SG Iron. *Inter Metalcast* **16**, 106–118 (2022). <https://doi.org/10.1007/s40962-021-00605-8>
 43. J. Lacaze, Trace elements and graphite shape degeneracy in nodular graphite cast irons. *Inter Metalcast* **11**, 44–51 (2017). <https://doi.org/10.1007/s40962-016-0115-6>
 44. G. Alonso, P. Larrañaga, D.M. Stefanescu et al., Kinetics of nucleation and growth of graphite at different stages of solidification for spheroidal graphite iron. *Inter Metalcast* **11**, 14–26 (2017). <https://doi.org/10.1007/s40962-016-0094-7>
 45. J.M. Tartaglia, R.B. Gundlach, G.M. Goodrich, Optimizing structure-property relationships in ductile iron. *Inter Metalcast* **8**, 7–38 (2014). <https://doi.org/10.1007/BF03355592>
 46. K. Jalava, K. Soivio, J. Laine et al., Effect of silicon and microstructure on spheroidal graphite cast iron thermal conductivity at elevated temperatures. *Inter Metalcast* **12**, 480–486 (2018). <https://doi.org/10.1007/s40962-017-0184-1>
 47. S.N. Lekakh, Communication: characterization of spatial distribution of graphite nodules in cast iron. *Inter Metalcast* **11**, 743–748 (2017). <https://doi.org/10.1007/s40962-016-0128-1>
 48. D. Franzen, B. Pustal, A. Bührig-Polaczek, Influence of Graphite-Phase Parameters on the Mechanical Properties of High-Silicon Ductile Iron. *Inter Metalcast* (2022). <https://doi.org/10.1007/s40962-022-00761-5>
 49. J. Laine, K. Jalava, J. Vaara et al., The mechanical properties of ductile iron at intermediate temperatures: the effect of silicon content and pearlite fraction. *Inter Metalcast* **15**, 538–547 (2021). <https://doi.org/10.1007/s40962-020-00473-8>
 50. J. Laine, A. Leppänen, K. Jalava et al., Ductile iron optimization approach for mechanically and thermally loaded components. *Inter Metalcast* **15**, 962–968 (2021). <https://doi.org/10.1007/s40962-020-00529-9>
 51. C. Hartung, R. Logan, A. Plowman et al., Research on solution strengthened ferritic ductile Iron (SSFDI)

- structure and properties using different treatment and inoculation materials. *Inter Metalcast* **14**, 1195–1209 (2020). <https://doi.org/10.1007/s40962-020-00469-4>
52. I. Pereira, G. Alonso, V. Anjos et al., The influence of alloying elements on damping capacity of nodular cast irons for braking system components. *Inter Metalcast* **14**, 802–808 (2020). <https://doi.org/10.1007/s40962-020-00426-1>
 53. D. Franzen, B. Pustal, A. Bührig-Polaczek, Mechanical properties and impact toughness of molybdenum alloyed ductile iron. *Inter Metalcast* **15**, 983–994 (2021). <https://doi.org/10.1007/s40962-020-00533-z>
 54. Y.S. Jang, M. Phaniraj, D.I. Kim et al., Effect of aluminum content on the microstructure and mechanical properties of hypereutectoid steels. *Metall Mater Trans A* **41**, 2078–2084 (2010). <https://doi.org/10.1007/s11661-010-0233-3>
 55. A. Shayesteh-Zeraati, H. Naser-Zoshki, A.R. Kiani-Rashid, Microstructural and mechanical properties (hardness) investigations of Al-alloyed ductile cast iron. *J. Alloys Compd.* **500**, 129–133 (2010). <https://doi.org/10.1016/j.jallcom.2010.04.003>
 56. A.R. Kiani-Rashid, Influence of austenitising conditions and aluminium content on microstructure and properties of ductile irons. *J. Alloys Compd.* **470**, 323–327 (2009). <https://doi.org/10.1016/j.jallcom.2008.02.070>
 57. N. Haghdadi, B. Bazaz, H.R. Erfanian-Naziftoosi, A.R. Kiani-Rashid, Microstructural and mechanical characteristics of Al-alloyed ductile iron upon casting and annealing. *Int. J. Miner. Metall. Mater.* **19**, 812–820 (2012). <https://doi.org/10.1007/s12613-012-0633-z>
 58. M.M. Khalvan, M. Divandari, Microstructure of spheroidal graphite aluminum-alloyed cast irons (SGAACI) containing up to 7.5 wt% produced via in-mold process. *Inter Metalcast* **15**, 271–280 (2021)
 59. S.N. Lekakh, V.L. Richards, N. Medvedeva, Effect of Si segregation on low temperature toughness of ductile iron. *AFS Trans.* **120**, 319–327 (2012)
 60. A. Alhussein, M. Risbet, A. Bastien, J.P. Chobaut, D. Balloy, J. Favergeon, Influence of silicon and addition elements on the mechanical behavior of ferritic ductile cast iron. *Mater. Sci. Eng. A* **605**, 222–228 (2014). <https://doi.org/10.1016/j.msea.2014.03.057>
 61. Q. Cai, Z. Chen, C. Xu et al., Effect of elemental segregation on the microstructure and mechanical properties of heavy section compacted graphite iron. *Inter Metalcast* (2022). <https://doi.org/10.1007/s40962-022-00758-0>
 62. A. Bedolla-Jacuinde, E. Solis, B. Hernandez, Effect of niobium in medium alloyed ductile cast irons. *Int. J. Cast Met. Res.* **16**, 481–486 (2003). <https://doi.org/10.1080/13640461.2003.11819625>
 63. J. Lacaze, B. Sundman, An assessment of Fe-C-Si system. *Metall. Mater. Trans. A* **22**, 2211–2223 (1991). <https://doi.org/10.1007/BF02664987>
 64. L.L. Liu, Q.Q. Guo, Y. Niu, Transition between different oxidation modes of binary Fe–Si alloys at 600–800 °C in Pure O₂. *Oxid Met* **79**, 201–224 (2013). <https://doi.org/10.1007/s11085-012-9318-2>
 65. L.L. Liu, Q.Q.Y. guoNiu, Transition between different oxidation modes of binary Fe–Si Alloys at 600–800 °C in pure O₂. *Oxid. Met.* **79**, 201–224 (2013). <https://doi.org/10.1007/s11085-012-9318-2>
 66. P. Tomaszewicz, G.R. Wallwork, Observations of nodule growth during the oxidation of pure binary iron-aluminum alloys. *Oxid. Met.* **19**, 165–185 (1983). <https://doi.org/10.1007/BF00666643>
 67. R. Prescott, M.J. Graham, The oxidation of iron-aluminum alloys. *Oxid. Met.* **38**, 73–87 (1992). <https://doi.org/10.1007/BF00665045>
 68. A.R. Kiani Rashid, D.V. Edmonds, Oxidation behaviour of Al-alloyed ductile cast irons at elevated temperature. *Surf. Interface Anal.* **36**, 1011–1013 (2004). <https://doi.org/10.1002/sia.1825>
 69. M.A. Mendez, A. Arenas, R. Niklas, A. González, J.S. Conde, J.J.D. Damborenea, Effect of silicon and graphite degeneration on high-temperature oxidation of ductile cast irons in open air. *Oxid. Met.* **91**, 225–242 (2019). <https://doi.org/10.1007/s11085-018-9875-0>
 70. M.M. Ibrahim, A. Nofal, M.M. Mourad, Microstructure and hot oxidation resistance of SiMo ductile cast irons containing Si-Mo-Al. *Metall. and Mater. Trans. B.* **48**, 1149–1157 (2017). <https://doi.org/10.1007/s11663-016-0871-y>
 71. S.N. Lekakh, A. Bofah, L.A. Godlewski, M. Li, Effect of micro-structural dispersity of SiMo ductile iron on high temperature performance during static oxidation. *Metals* **12**, 661 (2022). <https://doi.org/10.3390/met12040661>
 72. S. Chandra-Ambhorn, T. Tummaporn, P. Jiradech, High temperature oxidation of Al-alloyed SiMo cast iron in CO₂-containing atmospheres. *AMR* **813**, 132–135 (2013). <https://doi.org/10.4028/www.scientific.net/amr.813.132>

Publisher's Note Springer Nature remains neutral with regard to jurisdictional claims in published maps and institutional affiliations.

Springer Nature or its licensor holds exclusive rights to this article under a publishing agreement with the author(s) or other rightsholder(s); author self-archiving of the accepted manuscript version of this article is solely governed by the terms of such publishing agreement and applicable law.